

Optohydrodynamics of soft fluid interfaces: Optical and viscous nonlinear effects

H. Chraïbi^{1,2,a}, D. Lasseux¹, R. Wunenburger², E. Arquis¹, and J.-P. Delville²

¹ Université Bordeaux I, TREFLE (UMR CNRS 8508), Esplanade des Arts et Métiers, 33405 Talence Cedex, France

² Université Bordeaux I, CPMOH (UMR CNRS 5798), 351 cours de la Libération, 33405 Talence Cedex, France

Received: 9 February 2010

Published online: 24 May 2010 – © EDP Sciences / Società Italiana di Fisica / Springer-Verlag 2010

Abstract. Recent experimental developments showed that the use of the radiation pressure, induced by a continuous laser wave, to control fluid-fluid interface deformations at the microscale, represents a very promising alternative to electric or magnetic actuation. In this article, we solve numerically the dynamics and steady state of the fluid interface under the effects of buoyancy, capillarity, optical radiation pressure and viscous stress. A precise quantitative validation is shown by comparison with experimental data. New results due to the nonlinear dependence of the optical pressure on the angle of incidence are presented, showing different morphologies of the deformed interface going from needle-like to finger-like shapes, depending on the refractive index contrast. In the transient regime, we show that the viscosity ratio influences the time taken for the deformation to reach steady state.

1 Introduction

Optical waves are an interesting and promising alternative to pure electric [1] and magnetic fields [2] to produce mechanical stress on fluid interfaces and deform them.

When focused light propagates through an interface separating two fluids of different refractive indices, photon momentum, which linearly depends on the refractive index, experiences a jump at the interface. This momentum jump induces a radiation pressure on the interface that acts towards the fluid of lowest optical index whatever the direction of propagation of the optical wave.

This surprising invariance property was first evidenced in the experiments of Ashkin and Dziedzic [3]. Their work was an attempt at giving an experimental answer to the Abraham-Minkowski controversy about light momentum's expression in a dielectric. The controversy arises due to Abraham's and Minkowski's predictions disagreeing as to whether the momentum carried by an electromagnetic field is increased (Minkowski) or decreased (Abraham) by the presence of a refractive medium. Ashkin and Dziedzic concluded that light momentum was consistent with Minkowski formalism (see [4] for a recent review on light momentum).

The deflection of the interface towards the less refractive fluid was later confirmed by Zhang and Chang [5] who used a pulsed laser wave to deform a water droplet and observed, immediately after the pulse, an oscillation of the interface leading to an emission of microdroplets at

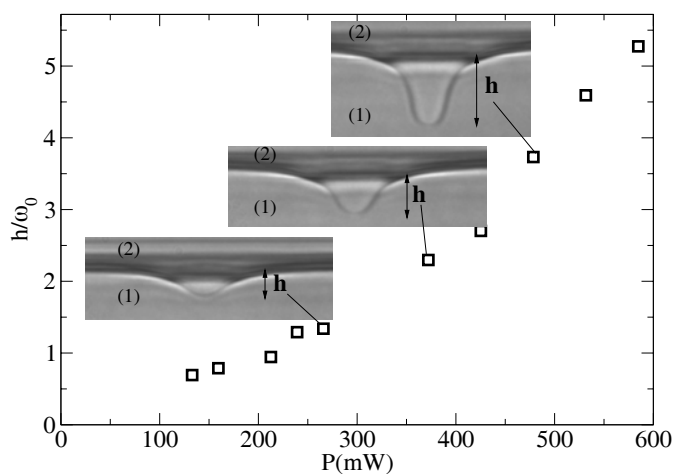


Fig. 1. Nonlinear variation of the height h (scaled by the beam radius $\omega_0 = 7.5 \mu\text{m}$) of the deformed interface versus the incident beam power P . The laser wave propagates upwards. The pictures correspond to $P = 265, 372$ and 478 mW. Interfacial tension is $\sigma = 5 \cdot 10^{-7}$ N/m, refractive index contrast is $n_2 - n_1 = 0.012$ and density contrast is $\rho_1 - \rho_2 = 24.7$ kg/m³.

the rear of the drop at large pulse energy. More recently, Casner and Delville [6] used the soft interface separating two near-critical liquid phases in order to reduce by several orders of magnitude the effect of interfacial tension and thus to significantly enhance the amplitude of interface deformations. Stationary deformations of large aspect ratio were observed [7] as illustrated in fig. 1.

^a e-mail: h.chraïbi@cpmoh.u-bordeaux1.fr

The radiation pressure effects open interesting perspectives for applications in many different fields:

- i) interface rheology first, with measurements of surface and interfacial tension at small scale [8,9], and microrheology characterization [10,11];
- ii) adaptive optics and holography with light actuation of reconfigurable fluid lenses [3,12,13] and interface relief gratings [14];
- iii) droplet cavity lasing [15];
- iv) surface relief micropatterning by extending electrical field approaches [16] to optics.

While experiments have highlighted a rich phenomenology, the complete understanding of the physics of interface deformation induced by an optical wave is still in its infancy. This task is indeed made difficult by the coupling between the shape of the interface and the optical radiation pressure distribution as well as the dependence of the interface shape on buoyancy, capillarity, viscosity and optical properties of the fluids. While some effort has been dedicated to the description of buoyancy effects on equilibrium interface deformations of small amplitude [17] (*i.e.* linear regime where the deformation height varies linearly with the beam power), very few studies have been performed to describe large amplitude deformations [18,19].

The aim of this paper is to investigate numerically the statics and dynamics of these large deformations for a wide range of refractive index contrasts, from very soft interfaces (near-critical systems $\sigma \sim 10^{-4}$ mN/m) to more usual pairs of fluids (water/air, for instance, $\sigma \sim 10$ – 100 mN/m). In essence, it is shown that the underlying physics can be explained by the nonlinear dependence of the radiation pressure on Snell-Descartes angles of refraction. It is further shown that the transient shape of the deformation exhibits a transition at a characteristic time which depends on the viscosity ratio.

Our analysis is organized as follows. The physical model for interface deformation is presented in sect. 2. In sect. 3, we first validate the computation algorithm through a successful comparison with experimental results. Finally an analysis of the refractive index contrast and viscous effects is performed showing new important features in both the unsteady and steady states in the nonlinear regime of deformation, *i.e.* when the equilibrium hump height has a nonlinear variation with the excitation amplitude.

2 Governing equations and numerical resolution

2.1 Physical model

We investigate the deformation of an initially horizontal stationary liquid-liquid interface, induced by the optical radiation pressure due to a continuous Gaussian laser beam of power P and radius (also called beam waist) ω_0 . Physical properties of the liquids (denoted 1 for the bottom and 2 for the top) are their refractive indices n_1, n_2 ,

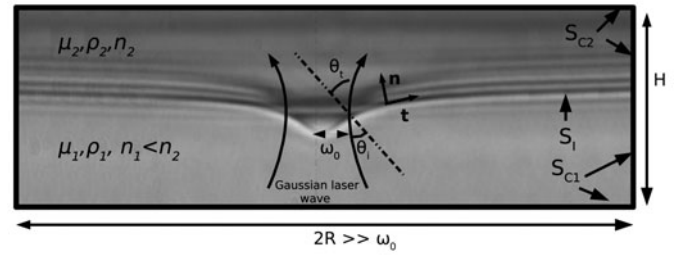


Fig. 2. Configuration and notations considered for simulations illustrated using an experimental liquid-liquid interface deformation driven by a focused laser wave propagating upward. $n_2 - n_1 = 0.011$, $\rho_1 - \rho_2 = 22$ kg/m³, $\sigma = 3.6 \cdot 10^{-7}$ N/m; $\omega_0 = 5.3 \mu\text{m}$; $P = 240$ mW. S_I , S_{C1} and S_{C2} , respectively, denote the interface and the solid walls in fluids 1 and 2.

viscosities μ_1, μ_2 and densities ρ_1, ρ_2 . The interfacial tension is denoted by σ . The fluids are enclosed in a cylindrical cell of radius $R \gg \omega_0$ and total height $H \gg \omega_0$.

Considering axisymmetry along the beam propagation axis z , the cylindrical coordinates $(\mathbf{e}_r, \mathbf{e}_\alpha, \mathbf{e}_z)$ with origin O located at the intersection of the beam axis with the initial flat interface are chosen for this study. A point \mathbf{x} is thus referenced by the space coordinates (r, α, z) . The configuration is summarized in fig. 2.

2.1.1 The optical radiation pressure

We consider the fluids as two nonabsorbing dielectric media with different refractive indices n , separated by an interface of arbitrary shape. The indices i and t refer to incidence and transmission, and θ_i and θ_t are, respectively, the Snell incident and transmission angles (see fig. 2). They can be expressed as $\theta_i = \arctan(\frac{dz}{dr})$ and $\theta_t = \arcsin((1 - \delta) \sin \theta_i)$, where $\delta = \frac{n_2 - n_1}{n_2}$ is the relative index contrast and $z = z(r)$ is the interface equation. Since the photon momentum depends on the refractive index, light momentum is not conserved when the beam crosses the interface separating these two dielectrics. The resulting discontinuity in momentum gives birth to the radiation pressure applied to the interface. If \mathbf{t} and \mathbf{n} refer to the tangent and normal directions to the interface at the location where the light impinges the interface, ν_0 represents the optical wave frequency, h_0 the Planck constant and c the light speed in vacuum, the photon momentum balance can be deduced from the fact that:

i) an incident photon gives the momentum $(n_1 h_0 \nu_0 / c)(\sin \theta_i \mathbf{t} + \cos \theta_i \mathbf{n})$ to the interface, ii) a reflected photon carries the momentum $(n_1 h_0 \nu_0 / c)(\sin \theta_i \mathbf{t} - \cos \theta_i \mathbf{n})$ away from the interface and iii) a transmitted photon picks the momentum $(n_2 h_0 \nu_0 / c)(\sin \theta_t \mathbf{t} + \cos \theta_t \mathbf{n})$ to the interface. By denoting N the number of photons impinging on the interface per unit time and unit interfacial area and by denoting $R(\theta_i, \theta_t)$ and $T(\theta_i, \theta_t) = 1 - R(\theta_i, \theta_t)$, the classical Fresnel coefficients of reflection and transmission of electromagnetic energy for circularly polarized beams

are given by [20]

$$T(\theta_i, \theta_t) = \frac{2(1-\delta)\cos\theta_i\cos\theta_t}{((1-\delta)\cos\theta_i + \cos\theta_t)^2} + \frac{2(1-\delta)\cos\theta_i\cos\theta_t}{(\cos\theta_i + (1-\delta)\cos\theta_t)^2}. \quad (1)$$

We can express the momentum variation $d\mathbf{Q}$ of the incident beam on an interface element of area dS during the time dt as $d\mathbf{Q} = d\mathbf{Q}_t + d\mathbf{Q}_n$, *i.e.*

$$d\mathbf{Q} = d\mathbf{Q}_t + d\mathbf{Q}_n = [n_1 \sin\theta_i - (Rn_1 \sin\theta_i + Tn_2 \sin\theta_t)] \frac{Nh_0\nu_0}{c} dS dt \mathbf{t} + [n_1 \cos\theta_i - (-Rn_1 \cos\theta_i + Tn_2 \cos\theta_t)] \frac{Nh_0\nu_0}{c} dS dt \mathbf{n}. \quad (2)$$

Since $n_1 \sin\theta_i = n_2 \sin\theta_t$, then $d\mathbf{Q}_t = 0$. There is no momentum transfer parallel to the interface. Consequently, one has

$$d\mathbf{Q} = d\mathbf{Q}_n = n_1 \cos\theta_i \left(1 + R - \frac{\tan\theta_i T}{\tan\theta_t}\right) \frac{Nh_0\nu_0}{c} dS dt \mathbf{n}. \quad (3)$$

Classically, the laser intensity I is defined as $I = N_0 h_0 \nu_0$, where N_0 is the flux of photons through the beam section. Since the laser wave incidence angle on the interface is θ_i , one gets $N = N_0 \cos\theta_i$. We deduce that the optical radiation force acting on the interface per unit area dS , when the laser wave propagates from the less to the more refractive fluid, \mathbf{II}^{-+} , is normal to the interface and given by

$$\mathbf{II}^{-+}(r) = n_1 \cos^2\theta_i \left(1 + R - \frac{\tan\theta_i T}{\tan\theta_t}\right) \frac{I(r, z)}{c} \mathbf{n}, \quad (4)$$

where \mathbf{II}^{-+} is the radiation pressure.

When the beam is weakly focused, the z dependence of the beam radius can be neglected, yielding

$$I(r, z) \approx I(r) = \frac{2P}{\pi\omega_0^2} e^{-2(r/\omega_0)^2}. \quad (5)$$

In fig. 3, we have represented $\mathbf{II}^{-+}(\theta_i)$ normalized by $\mathbf{II}^{-+}(\theta_i = 0)$, the radiation pressure at normal incidence, *versus* the incidence angle θ_i for different values of the relative index contrast $\delta = \frac{n_2 - n_1}{n_2} = 0.01, 0.02$ and 0.4 .

First, we can see that the normalized radiation pressure decreases with θ_i and vanishes at tangential incidence ($\theta_i = 90^\circ$). Second, $\mathbf{II}^{-+}(\theta_i)$ is independent of the incidence angle when $\theta_i < 20^\circ$, a situation that corresponds to the regime of quasi-normal incidence. For $\theta_i > 20^\circ$, $\mathbf{II}^{-+}(\theta_i)$ decreases significantly beyond a certain value of θ_i which increases as δ decreases. Physically, this illustrates that the radiation pressure, *i.e.* the momentum jump of photons at the interface, is less sensitive to the incidence angle when the two fluids tend to refractive index matching ($\delta \rightarrow 0$). As detailed below, the coupling between radiation pressure and interface deformation ($\tan\theta_i = \frac{dz}{dr}$), is the major physical feature that explains both the dynamics and statics of the interface deformation.

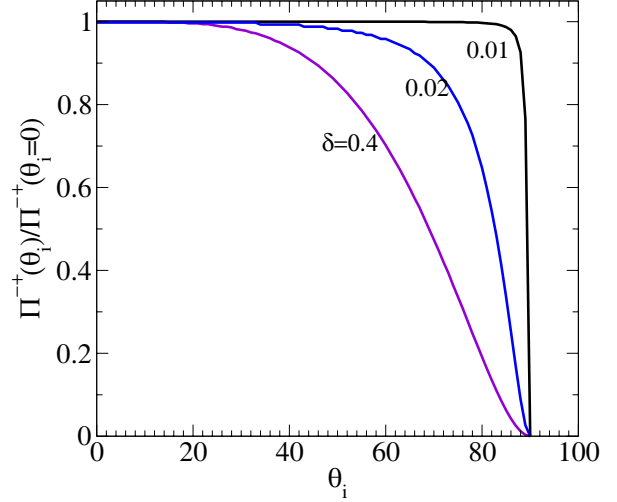


Fig. 3. Variation of the radiation pressure normalized by its value at normal incidence, *versus* the incidence angle for different values of the relative index contrast $\delta = \frac{n_2 - n_1}{n_2}$.

2.1.2 Governing equations

Since the Reynolds number associated with the flows under consideration is always small compared to unity ($\text{Re} = \frac{U\omega_0\rho}{\mu} \simeq 10^{-3}$, $\mu \simeq 10^{-3}$ Pa.s, $\rho \simeq 10^3$ kg/m³, $\omega_0 \simeq 10$ μm and $U \simeq 10^{-4}$ m/s a characteristic velocity of the flow), both fluids obey the mass conservation and Stokes equations.

Their dynamics are coupled through stress balance in addition to the continuity of velocity at the interface denoted S_I . The motion of the interface is described following a Lagrangian approach. Using w_0 as a reference length, $U_0 = \frac{2\sigma}{\mu_1 + \mu_2}$ as a reference velocity and $p_{i0} = \frac{\mu_i U_0}{\omega_0}$, $i = 1, 2$ as a reference pressure in fluid i , the axisymmetric dimensionless boundary value problem can thus be expressed as

$$\nabla \cdot \mathbf{u}_i = 0, \quad i = 1, 2, \quad (6)$$

$$\mathbf{0} = -\nabla p_i + \Delta \mathbf{u}_i, \quad i = 1, 2, \quad (7)$$

$$\frac{2}{1 + \zeta} (\zeta \mathbf{T}_1 \cdot \mathbf{n} - \mathbf{T}_2 \cdot \mathbf{n}) = (\kappa(r) + \mathbf{II}(r) - \text{Bo} z) \mathbf{n}, \quad \mathbf{x} \text{ on } S_I, \quad (8)$$

$$\mathbf{u}_1 = \mathbf{u}_2 \text{ on } S_I, \quad \mathbf{u}_1 = \mathbf{0} \text{ on } S_{C1}, \quad \mathbf{u}_2 = \mathbf{0} \text{ on } S_{C2}, \quad (9)$$

$$\frac{d\mathbf{x}}{dt} = \mathbf{u}(\mathbf{x}) \quad \text{on } S_I, \quad (10)$$

\mathbf{u}_i , p_i are, respectively, the dimensionless velocity and pressure in each fluid, while $\mathbf{T}_i = -p_i \mathbf{I} + (\nabla \mathbf{u}_i + {}^t \nabla \mathbf{u}_i)$ is the dimensionless stress tensor and $\zeta = \mu_1/\mu_2$ the viscosity ratio. $\kappa(r) = \frac{1}{r} \frac{d}{dr} \frac{r \frac{dz}{dr}}{\sqrt{1 + \frac{dz}{dr}^2}}$ is twice the mean curvature of the axisymmetric interface in cylindrical coordinates, $\mathbf{II}(r) = \frac{\omega_0}{\sigma} \mathbf{II}^{-+}(r)$ is the dimensionless radiation pressure where \mathbf{II}^{-+} is given by eq. (4) and $\text{Bo} = (\rho_1 - \rho_2)g\omega_0^2/\sigma$

is the gravitational Bond number which quantifies the relative magnitude of buoyancy to capillary effects for small deformation amplitude. A detailed investigation dedicated to the gravitational effects was proposed in a previous work, for small deformation amplitudes [17,21]. Since Bo is typically in the range 10^{-3} – 10^{-1} for fluids commonly encountered, buoyancy can reasonably be neglected compared to the other forces and will not be discussed in the present paper.

In order to quantify effects of the laser wave on the interface deformation, it is convenient to define the optical to Laplace pressure ratio. This ratio π_0 taken at $r = 0$ ($\theta_i = \theta_t = 0$), is defined as

$$\pi_0 = |\Pi(r = 0)| = \frac{4P}{\pi c \omega_0 \sigma} \frac{n_1(n_2 - n_1)}{(n_2 + n_1)} \quad (11)$$

and can be considered as the optical Bond number.

2.2 Integral formulation and algorithm

Since solutions to the Stokes problem can be formulated in terms of Green's functions [22], we rewrite the governing equations as a system of integral equations over the boundaries of the computational domain. Once boundary conditions on the interface S_I and solid boundaries S_{C1} and S_{C2} in contact with fluid 1 and 2 are used (see fig. 2), the two-phase Stokes problem can be written in the following compact form:

$$\begin{aligned} \frac{1 + \zeta}{2} \mathbf{u}(\mathbf{x}) &= \int_{S_I} \mathbf{U} \cdot \mathbf{n} (\kappa(r_y) + \Pi(r_y) - Bo z(r_y)) dS_y \\ &+ (1 - \zeta) \int_{S_I} \mathbf{n} \cdot \mathbf{K} \cdot \mathbf{u} dS_y + \zeta \int_{S_{C1}} \mathbf{U} \cdot (\mathbf{T}_1 \cdot \mathbf{n}) dS_y \\ &- \int_{S_{C2}} \mathbf{U} \cdot (\mathbf{T}_2 \cdot \mathbf{n}) dS_y. \end{aligned} \quad (12)$$

Here, \mathbf{U} and \mathbf{K} are Green's kernels for velocity and stress respectively and are given by [22]

$$\mathbf{U}(\mathbf{d}) = \frac{1}{8\pi} \left(\frac{1}{d} \mathbf{I} + \frac{\mathbf{d}\mathbf{d}}{d^3} \right), \quad (13)$$

$$\mathbf{K}(\mathbf{d}) = -\frac{3}{4\pi} \left(\frac{\mathbf{d}\mathbf{d}\mathbf{d}}{d^5} \right), \quad (14)$$

where $\mathbf{d} = \mathbf{x} - \mathbf{y}$, $\mathbf{y}(r_y, z_y)$ is the integration point. In eq. (12), the first term on the right-hand side describes the flow contribution from interfacial tension, radiation pressure and gravity, whereas the second term accounts for shear rates contrast on the interface. This term vanishes when $\zeta = 1$. The third and fourth terms account for shear occurring on S_{C1} and S_{C2} as a result of the no-slip boundary condition.

Velocities on the interface as well as stress over all the boundaries S_I , S_{C1} and S_{C2} are determined by solving the discrete form of this equation using a Boundary Element Method (BEM). Details on the BEM applied to two-phase axisymmetric flow can be found in the review by Tanzosh

et al. [23] on the solution of free surface flow using this technique. The BEM reveals itself to be an excellent tool to solve interfacial flow problems with high resolution as reported in the analysis of flow involving electric and magnetic fields [2] or buoyancy [24,25].

The solution requires first the discretization of all the boundaries S_I , S_{C1} and S_{C2} . Due to the integral formulation and axial symmetry, the problem is reduced to one dimension and only line boundaries need to be discretized. In this work, the mesh is made of constant boundary elements, *i.e.* line segments with centered nodes. Azimuthal integration of eq. (12) is performed analytically [26,27] reducing eq. (12) to a line integration which is finally performed using Gauss quadratures [28]. Elliptic integrals resulting from the azimuthal integration are evaluated using power series expansions [29].

The fluid-fluid interface S_I is parameterized in terms of arc length and is approximated by local cubic splines to remesh the interface during its deformation, so that the curvature can be accurately computed. Distribution and number of points are adapted to the shape of the interface, so that the concentration of elements is higher in regions where the variation of curvature of the interface is large. The number of mesh points is about 70 for a typical computation of a small interface deformation. The solid boundaries S_{C1} and S_{C2} are meshed using about 40 uniformly distributed points. An increase in the mesh resolution for the interface and the solid boundaries does not show any change in the results.

The motion of the interface is followed using the kinematic condition (10) which is discretized using an explicit first-order Euler time scheme. A typical computation begins with a flat interface at rest. The laser beam is switched on at $t = 0$, and the interface deforms towards fluid 1 of the smallest refractive index. Computation stops when an equilibrium state is reached ($\mathbf{v} \cdot \mathbf{n}|_{S_I} \rightarrow 0$). The time step is chosen to be about 20 times smaller than the reference time $\tau_0 = \frac{\omega_0}{U_0}$.

3 Results

3.1 Comparison with experiments

In this section, we compare numerical predictions to experimental data giving both the time evolution of the interface and the steady-state hump heights and interface shapes for various laser illuminations and fluid properties.

The experimental fluids correspond to a phase-separated near-critical water-in-oil micellar mixture contained in a thermo-regulated spectroscopic cell at temperature T , for which a very low interfacial tension can be achieved. Details on how the solution is prepared can be found in [6]. Above the critical temperature $T_c = 308$ K, two distinct fluid phases 1 and 2 of different compositions coexist with densities $\rho_1 > \rho_2$ and refractive indices $n_1 < n_2$. A vertical upward Gaussian beam from a continuous wave Ar⁺ laser operating at wavelength 514.5 nm

Table 1. Typical values of fluid properties for different values of $T - T_c$.

| $T - T_c$ (K) | σ (mN/m) | $n_2 - n_1$ | δ | $\rho_1 - \rho_2$ (kg/m ³) | $\mu_1 - \mu_2$ (Pa s) |
|---------------|---------------------|-------------|----------|--|------------------------|
| 2 | $1.8 \cdot 10^{-4}$ | 0.0097 | 0.0066 | 19 | $3.1 \cdot 10^{-4}$ |
| 4 | $4.0 \cdot 10^{-4}$ | 0.012 | 0.0083 | 24 | $3.9 \cdot 10^{-4}$ |
| 6 | $7.0 \cdot 10^{-4}$ | 0.014 | 0.0095 | 27 | $4.4 \cdot 10^{-4}$ |
| 8 | $1.0 \cdot 10^{-3}$ | 0.015 | 0.010 | 30 | $4.9 \cdot 10^{-4}$ |
| 10 | $1.3 \cdot 10^{-3}$ | 0.016 | 0.011 | 32 | $5.2 \cdot 10^{-4}$ |
| 15 | $2.2 \cdot 10^{-3}$ | 0.018 | 0.013 | 36 | $6.0 \cdot 10^{-4}$ |
| 20 | $3.2 \cdot 10^{-3}$ | 0.020 | 0.014 | 40 | $6.5 \cdot 10^{-4}$ |

is then focused at normal incidence onto the flat fluid-fluid interface. More exhaustive experimental details on the configuration and protocol as well as on the determination of the sample properties used here were reported earlier [17,19].

As already demonstrated [30], the thermophysical properties of the fluids can be evaluated using asymptotic scaling laws of near critical phenomena [31].

Assuming that the coexistence curve is symmetric *versus* the critical concentration φ_c , the micellar concentration in each phase φ_i ($i = 1, 2$) can be estimated by

$$\varphi_1 = \varphi_c + \frac{\Delta\varphi}{2}, \quad (15)$$

$$\varphi_2 = \varphi_c - \frac{\Delta\varphi}{2}, \quad (16)$$

with $\varphi_c = 0.11$ and

$$\Delta\varphi = \Delta\varphi_c \left(\frac{T - T_c}{T_c} \right)^{0.325}, \quad (17)$$

with $\Delta\varphi_c = 0.5$.

The density of each phase ρ_i , $i = 1, 2$ can be written as a function of φ_i ,

$$\rho_i = \rho_{\text{mic}}\varphi_i + \rho_{\text{cont}}(1 - \varphi_i), \quad (18)$$

where $\rho_{\text{mic}} = 1045 \text{ kg m}^{-3}$ and $\rho_{\text{cont}} = 850 \text{ kg m}^{-3}$ are the densities of the micelles and continuous phases, respectively.

Because the average distance between two micelles is small compared to the wavelength of the laser wave, the mixture can be regarded as homogeneous from the electromagnetic point of view. Thus, the relative dielectric permittivity $\epsilon_i = n_i^2$ of the mixture is [32]

$$\epsilon_i(\varphi_i) = \varphi_i\epsilon_{\text{mic}} + (1 - \varphi_i)\epsilon_{\text{cont}} - \frac{\varphi_i(1 - \varphi_i)(\epsilon_{\text{mic}} - \epsilon_{\text{cont}})^2}{3(\varphi_i\epsilon_{\text{mic}} + (1 - \varphi_i)\epsilon_{\text{cont}})}, \quad (19)$$

along with $\epsilon_{\text{mic}} = 1.86$ and $\epsilon_{\text{cont}} = 2.14$, ϵ_{mic} and ϵ_{cont} being the relative permittivity of the micelles and the continuous oil phase, respectively.

Since concentrations are weak, we use Einstein's relation to estimate the dynamic viscosity μ_i of each phase:

$$\mu_1 = \mu_0 \left(1 + 2.5 \frac{\Delta\varphi}{2} \right), \quad (20)$$

$$\mu_2 = \mu_0 \left(1 - 2.5 \frac{\Delta\varphi}{2} \right), \quad (21)$$

with $\mu_0 = 1.269 \text{ mPa s}$.

Finally, the interfacial tension is written as

$$\sigma = \sigma_0 \left(\frac{T - T_c}{T_c} \right)^{1.26}, \quad (22)$$

with $\sigma_0 = 10^{-4} \text{ N/m}$.

Since fluids are assumed to be transparent (the optical absorption is $3 \cdot 10^{-4} \text{ cm}^{-1}$), the action of light on the interface can be considered as a pure mechanical stress, allowing us to discard heat dissipation and thermocapillary effects and to consider all liquid properties (ρ_i , μ_i , n_i and σ) as constant and independent of field strength.

Typical values of the fluids properties are given in table 1.

3.1.1 Unsteady regime

One of the first studies of the dynamics of free surface flow induced by the radiation pressure has been performed by Ostrovskaya *et al.* [33]. It consisted in solving the unsteady, linearized momentum and mass conservation equations in cylindrical coordinates with a linearized boundary condition at the free surface. In a recent paper, Wunenburg *et al.* [21] generalized this approach to a liquid-liquid interface where the liquids have identical viscosities. In particular, it was shown that for small deformation amplitudes (where $h \lesssim 1$ and $\pi_0 \lesssim 1$), the interface dynamics is accurately described by a linear theory of overdamped interfacial waves [21]. For linearized radiation and Laplace pressures (*i.e.* $\frac{dz}{dr} \ll 1$), the following expression of the dimensionless time evolution of the interface hump height was predicted to be:

$$h_{\text{lin}}(t) = z(r = 0, t) = \frac{\pi_0}{4} \int_0^\infty e^{-k^2/8} \frac{1}{1 + \text{Bo}/k^2} \left[1 - \exp\left(-t \frac{1 + \text{Bo}/k^2}{4} k\right) \right] \frac{dk}{k}. \quad (23)$$

This prediction has proven to be accurate when compared to experimental data over a wide range of fluid properties.

Note that the equilibrium solution can be easily deduced when $t \rightarrow \infty$,

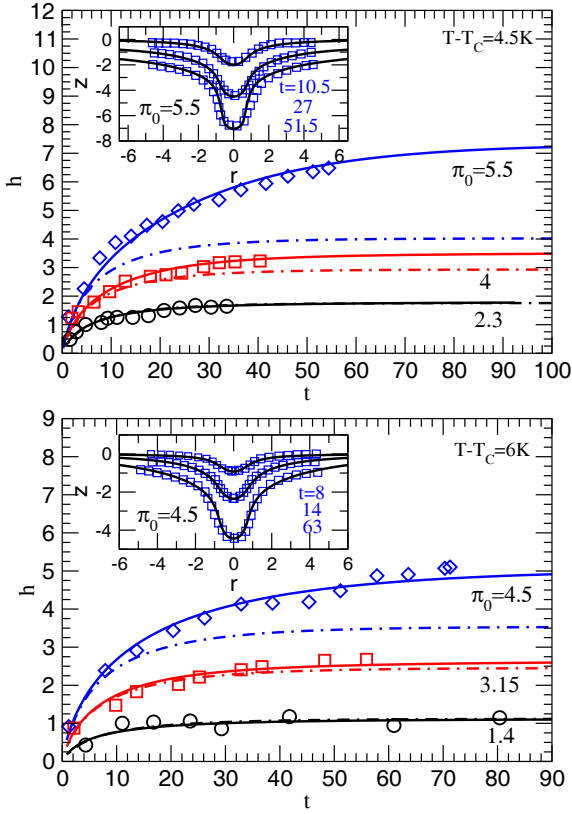


Fig. 4. Time evolution of the interface hump height for $\omega_0 = 4.8 \mu\text{m}$. Experiments (symbols) are compared to numerical predictions (continuous lines) and linearized theory $h_{\text{lin}}(t)$ (dot-dashed lines). Top: $T - T_c = 4.5 \text{ K}$, $\delta = \frac{n_2 - n_1}{n_2} = 0.0086$ and $\zeta = \frac{\mu_1}{\mu_2} = 1.37$. Bottom: $T - T_c = 6 \text{ K}$, $\delta = 0.0095$ and $\zeta = 1.42$. Time t is dimensionless (reference time is $\tau_0 = \frac{\omega_0}{U_0}$). The inset shows the interface shape at different times.

$$h_{\infty, \text{lin}} = \frac{\pi_0}{8} e^{\frac{B_0}{8}} E_1\left(\frac{B_0}{8}\right), \quad (24)$$

where $E_1(x)$ is the exponential integral $\int_x^\infty \frac{e^{-k}}{k} dk$.

Comparison of numerical predictions with experimental results of the time evolution of the hump height for large beam illumination ($\pi_0 > 1$) is depicted in fig. 4. Very good agreement on hump dynamics and profiles (inset) is illustrated for two sets of experimental data ($T - T_c = 4.5 \text{ K}$ and $T - T_c = 6 \text{ K}$) and for different values of beam illuminations ranging from $\pi_0 \sim 1.5$ to 5.5.

On the same figure, we have represented the time-dependent solution given by the linear model (eq. (23)) when the optical radiation pressure and capillary terms are linearized. This linearization strongly underpredicts both the steady hump height (for $T - T_c = 4.5 \text{ K}$ and $\pi_0 = 5.5$, $h_{\infty, \text{lin}} = 4$ while $h = 7.2$) and the time necessary to reach 99% of the steady hump height ($\tau_{99, \text{lin}} = 40$ while $\tau_{99} = 100$). This shows that the complete forms of both the radiation pressure and capillary pressure terms are necessary to yield an accurate description of the interface dynamics.

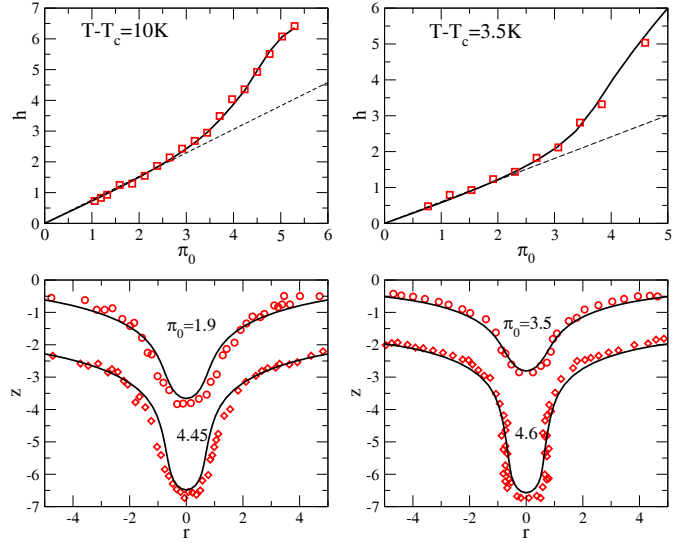


Fig. 5. Top: numerical and experimental interface steady hump height variation with the optical-to-Laplace pressure ratio π_0 . Dashed lines represent the linear prediction $h_{\infty, \text{lin}}$. Bottom: steady-state interface profiles for different π_0 ($\omega_0 = 5.3 \mu\text{m}$) (profiles were arbitrarily shifted in the z -direction). In all graphs, symbols and continuous lines represent experimental data and numerical solutions, respectively. Left: $T - T_c = 10 \text{ K}$, $\delta = \frac{n_2 - n_1}{n_2} = 0.011$. Right: $T - T_c = 3.5 \text{ K}$, $\delta = 0.008$.

3.1.2 Steady state

In fig. 5, we compare the experimental results for the stationary interface hump height h versus π_0 to the computed predictions. These data were obtained at $T - T_c = 10 \text{ K}$ and $T - T_c = 3.5 \text{ K}$. Experimental profiles of the interface are also compared to the steady profiles obtained numerically for π_0 ranging from 2 to 4.5. These results clearly show that the numerical resolution gives an excellent prediction of the interface hump height and profile providing a quantitative validation of our model in both the linear ($\pi_0 \sim 2$) and nonlinear ($\pi_0 \sim 4.5$) regime.

Considering the accuracy of our calculations, we now extend the numerical investigation to a range of values of the relative index contrast $\delta = \frac{n_2 - n_1}{n_2}$ and viscosity ratio $\zeta = \frac{\mu_1}{\mu_2}$ that goes far beyond the existing experimental data. This will highlight original features for both the steady state and dynamics of the interface.

3.2 Optical effects

The near-critical fluid phases used in the experiments had a relative index contrast varying from $\delta = 0.0066$ for $T - T_c = 2 \text{ K}$ to $\delta = 0.015$ for $T - T_c = 25 \text{ K}$ featuring a very narrow range of variation of this parameter. Experimentally, it is possible to reach steady deformations with comparable aspect ratios using other couples of fluids such as Octane/Water with Span 80 or SDS as surfactants ($\sigma \sim 10^{-2} \text{ mN/m}$ and $\delta \sim 0.06$). Higher relative index contrasts $\delta \sim 0.35$, (Water+Lung surfactants)/Air

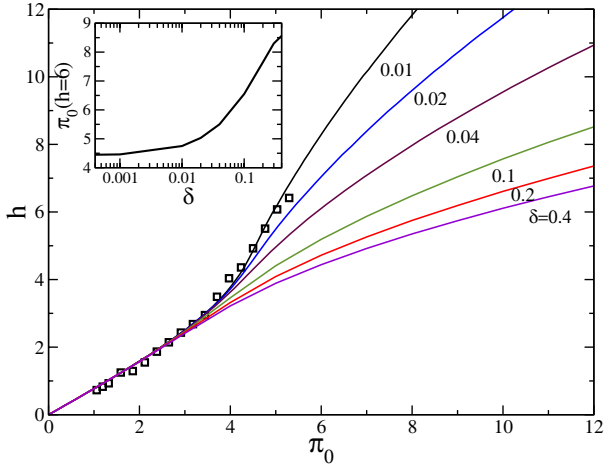


Fig. 6. Interface hump height variation with π_0 for different relative index contrasts $\delta = \frac{n_2 - n_1}{n_2}$. The square symbols are experimental data corresponding to $\delta = 0.01$. Inset: variation of π_0 needed to reach $h = 6$, as a function of δ .

interface ($\sigma \sim 10$ mN/m) can be achieved, although a beam power of approximately 10 W becomes necessary.

Given these experimental constraints, we investigate the role of δ in the range $10^{-5} < \delta < 0.4$ by means of numerical simulations in order to understand its effects on the deformation in the nonlinear regime.

In fig. 6, we have represented the variation of the steady-state interface hump height, h as a function of π_0 for several values of δ ranging from 0.01 to 0.4.

As shown above, for sufficiently small values of the optical illumination ($\pi_0 < 2$), h varies linearly with π_0 and has no dependence on δ .

In the nonlinear regime ($\pi_0 > 2$), h strongly depends on δ . For any given value of π_0 , h is larger when δ decreases. This is due to the fact that, for given π_0 and θ_i , $\Pi(\theta_i)$ is a decreasing function of δ (see fig. 3).

The inset of fig. 6 illustrates this statement. It shows that the value of π_0 needed to reach $h = 6$ as a function of δ decreases when decreasing δ . However, we can also notice a saturation of $\pi_0 = f(\delta)$. Indeed, when δ is getting very small, the radiation pressure becomes quasi-insensitive to the incidence angles θ_i (*i.e.* to the local slope $\frac{dz}{dr}$) except when θ_i is very close to 90° .

In fig. 7(a, b, c) we have represented the interface steady profile, for three values of δ : 10^{-5} , 0.01 and 0.4. The corresponding values of π_0 were chosen in order to obtain the same interface hump height $h \simeq 10$. It is noteworthy that the shape of the deformation in the nonlinear regime strongly depends on δ . At relatively large values of δ , (*e.g.* $\delta = 0.4$ in fig. 7a), the center part of the interface adopts a needle-like shape with a sharp tip. Decreasing δ (*e.g.* $\delta = 0.1$, see fig. 7b) widens and rounds off the tip, showing a bell shape, while the base of the deformation shrinks. More surprisingly, when the two fluids have almost the same refractive properties, a stable finger, nearly cylindrical with a round tip, is obtained (fig. 7c). This shape evolution corresponds to what is observed on the two pictures superimposed on fig. 7 and extracted from ex-

periments performed with near-critical phases. Figure 7d, obtained at $T - T_c = 20$ K ($\delta \simeq 0.014$) and $\pi_0 \sim 5.5$ shows that the interface adopts a bell shape while fig. 7e, obtained at $T - T_c = 2$ K ($\delta \simeq 0.0066$) and $\pi_0 \sim 9$, shows a nearly cylindrical finger.

These observations can be explained qualitatively by considering the balance of radiation and Laplace pressures. The finger shape ($\delta \rightarrow 0$) corresponds to a case where the radiation pressure is almost independent of the incidence angle (see fig. 3). This means that $\Pi(r) \simeq \pi_0 e^{-2r^2}$. Therefore, as only the capillary force balances the optical radiation pressure at steady state (we neglect the weak influence of gravity), we have $\kappa(r) \sim \Pi(r)$. This is confirmed in fig. 7h where the curvature profile shows an excellent agreement with the Gaussian profile (see fig. 7h).

The other shapes ($\delta = 0.1$ and $\delta = 0.4$) show that when the radiation pressure strongly depends on the incidence angle, the profile tends to a needle shape as the maximum of $\Pi(r)$ becomes more and more localized toward the tip ($r = 0$ and $\theta_i = 0$).

Consequently, one can tune the morphology of stationary nonlinear deformations by simply changing the refractive index contrast.

In the following, we show that the dynamics of the deformation has also a strong dependence on the relative index contrast δ .

In fig. 8, the time evolution of the hump height $h(t)$ is plotted for δ ranging from 10^{-4} to 0.4. We note that the transient regime is significantly longer when δ is closer to zero, *i.e.* when the fluids tend to match optically. This is explained in the left inset of this figure that shows the time variation of the radiation pressure integrated over the interface $|\int_{S_I} \Pi(r, t) \mathbf{n} dS| = 2\pi \int_0^{\frac{R}{\omega_0}} \Pi(r, t) r dr$ reduced by its initial value $2\pi \int_0^{\frac{R}{\omega_0}} \Pi(r, t = 0^+) r dr$. This ratio, called F , simply represents the time variation of the net optical force applied to the interface during the transient deformation. We can notice that this force quickly reaches its steady state value when $\delta = 0.4$, whereas the transient is much longer for $\delta = 0.01$. This observation can be explained qualitatively by considering the decrease of the radiation pressure with the incidence angle θ_i . As the deformation increases, θ_i increases along the interface, therefore the associated radiation pressure applied on the growing hump decreases locally for $\delta = 0.4$, while it remains quasi-unchanged for $\delta = 0.01$. The characteristic relaxation time of the optical force is smaller when increasing δ . As this force is the source of momentum transferred to the interface, the dynamics of the interface follows a similar behaviour with δ .

The right inset shows a characteristic time τ_{60} chosen arbitrarily at 60% of the equilibrium hump height as a function of δ . We can clearly see that τ_{60} increases when δ decreases, before reaching a saturation. This saturation is related to the weak dependence of $\Pi(r)$ on θ_i at small δ .

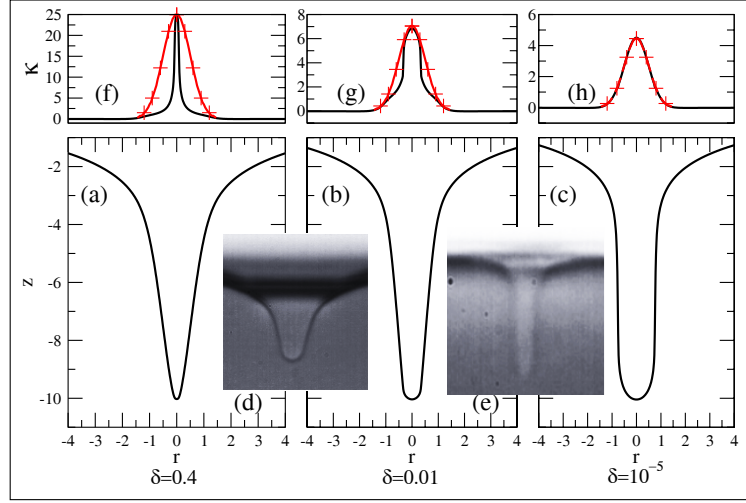


Fig. 7. Bottom (a, b, c): interface steady profiles for $\delta = 0.4, 0.01$ and 10^{-5} . π_0 is chosen to keep $h \simeq 10$. $Bo = 0.003$. Central pictures (d, e) were obtained from experiments with $Bo = 0.003$. Left picture (d): $T - T_c = 20$ K, $\delta \simeq 0.014$, $\pi_0 \sim 5.5$. Right picture (e): $T - T_c = 2$ K, $\delta \simeq 0.0066$ and $\pi_0 \sim 9$. Top (f, g, h): curvature of steady profile associated to the deformations. The line with (+) symbols is a Gaussian profile.

3.3 Viscous effects

By analogy with the analysis of the effects of refraction indices on the deformation, we now investigate the effect of the viscous ratio $\zeta = \frac{\mu_1}{\mu_2}$ on the transient behaviour of the deformation towards equilibrium. Equation (8) shows that the transient deformation depends on viscosities only through their ratio ζ .

In the case of the near-critical phases used in the experiments reported earlier, ζ was varying from 1.27 for $T - T_c = 2$ K to 1.76 for $T - T_c = 25$ K. As ζ was close to unity, no particular behaviour was observed in the transient regime.

It is however possible to imagine experiments with larger values of ζ . Using viscous Glucose-Water/Hexadecane or Glucose-Water/Toluene and appropriate surfactants would enable to obtain a viscosity ratio of $\zeta \sim 150$ with $\delta \sim 0.06$ and $\sigma \sim 10^{-2}$ mN/m still allowing large scale deformations using a continuous laser beam. A theoretical study would thus be a very useful predictive tool for the design of realistic future experiments. For this reason, we investigate the effect of the viscosity ratio in the two limit cases $\zeta = 200$ and $\zeta = 1/200$.

Figure 9 shows the evolution of the interface profile at different times for these two values of ζ , keeping $\delta = 0.1$, $Bo = 0.01$ and $\pi_0 = 15$.

In the case $\zeta = \frac{1}{200}$, we can observe a sharp transition from a bell shape ($t = 0.65$), characteristic of a small deformation amplitude, to a needle shape ($t = 4.7$). For $\zeta = 200$, we observe that the transition towards the needle shape occurs later, the tip of the interface showing a rounded shape between $t = 4.7$ and $t = 7.9$. This shape transition can be further characterized by analyzing the time dependence of the reduced curvature of the curvature at the tip, $\frac{\kappa^{(2)}(t)}{\kappa(t)} = \frac{\frac{1}{r} \frac{d}{dr} (r \frac{d\kappa(r,t)}{dr})|_{r=0}}{\kappa(r=0,t)} = \frac{\frac{d^2\kappa(r,t)}{dr^2}|_{r=0}}{\frac{d^2\kappa}{dr^2}|_{r=0}}$ shown

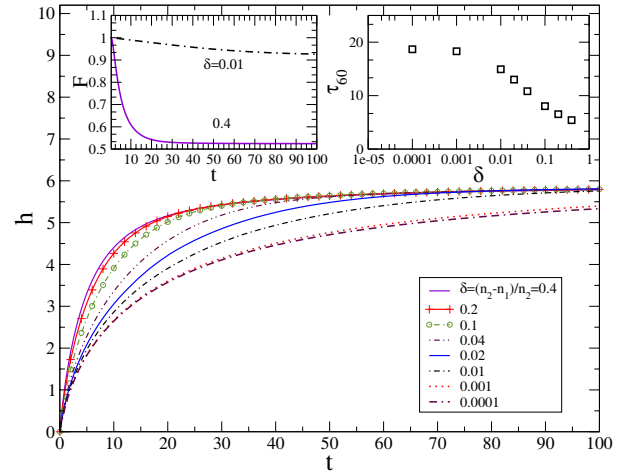


Fig. 8. Time evolution of the interface hump height for different values of δ . π_0 is chosen to keep $h \simeq 6$. $Bo = 0.005$. The left inset shows the time variation of the net radiation force acting on the interface $F(t)$ for $\delta = 0.4$ and $\delta = 0.01$ ($\zeta = \frac{\mu_1}{\mu_2} = 1$). The right inset shows the characteristic time τ_{60} taken for the hump height to reach 60% of its final steady value plotted against δ .

in fig. 9, $\frac{\kappa^{(2)}}{\kappa}$ being an indicator of the spatial variation of the curvature. In fact, a needle shape has a sharper curvature variation with r than a rounded shape (see fig. 7f and h), which means that $\frac{\kappa^{(2)}}{\kappa}$ is larger (in magnitude) for the needle shape. We observe in fig. 9 that, for a given value of ζ , $\frac{\kappa^{(2)}(t)}{\kappa(t)}$ initially increases until reaching a maximum at time τ_ζ ($\tau_{1/200} = 3.3$, $\tau_{200} = 9.5$) before decreasing toward the steady-state value. This maximum is a signature of the change of the shape evolution that switches from a round tip to a sharp one corresponding to a needle shape.

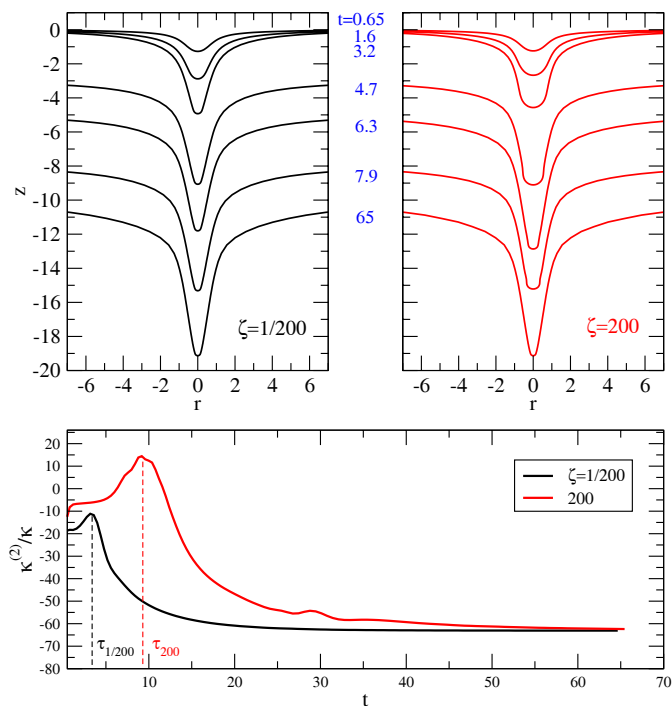


Fig. 9. Top: interface profiles at different times for two values of the viscosity ratio $\zeta = \frac{\mu_1}{\mu_2} = \frac{1}{200}$ (left) and $\zeta = 200$ (right). $\delta = 0.1$ and $\text{Bo} = 0.01$. Profiles were shifted vertically for clarity. Bottom: time evolutions of the corresponding reduced curvature of the curvature $\frac{\kappa^{(2)}(t)}{\kappa(t)} = \frac{d^2 \kappa(r,t)}{dr^2} \Big|_{r=0}$.

4 Conclusion

While quantitatively validated with experimental data in the nonlinear regime of deformation, our numerical resolution, based on a Boundary Element Method, showed that new morphologies of a soft fluid–fluid interface deformed by a continuous laser wave emerge when fluids become contrasted. In the nonlinear regime, where the radiation pressure and the height of the interface strongly depend on the relative refractive index contrast δ , we showed that the interface shape turns from a needle to a nearly cylindrical finger shape. In the transient regime, we predicted that the characteristic time of the deformation increases when decreasing δ before reaching a saturation. These results show the strong nonlinear coupling between the radiation pressure and the interface deformation in both transient and steady state. It was shown that the physical feature explaining these results lies in the dependence of the radiation pressure on the incidence angle. An original experimental evidence of this dependence can be achieved when the beam axis is not perpendicular to the initial flat interface. In this configuration, the interface hump is attracted in the direction of light propagation in the nonlinear regime of deformation (see fig. 10).

Finally, the influence of the viscosity ratio ζ has been investigated for large scale deformations. We showed that the transition time of the interface from its initial bell shape to the steady shape increases with ζ .

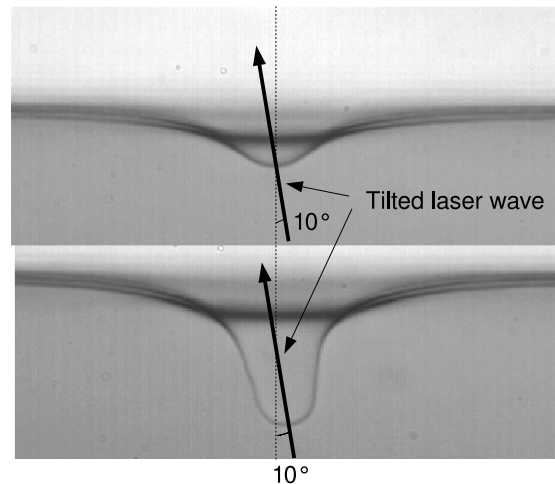


Fig. 10. Interface deformation with a tilted laser beam propagating upwards. Top: $P = 1$ W. Bottom $P = 1.7$ W. $\Delta n = 0.016$ and $\sigma = 1.4 \cdot 10^{-6}$ N/m. When the beam is tilted, incidence angles on one side of the deformation (here the left one) are larger than in the other side. When they are sufficiently small to consider radiation pressure as constant all over the interface, the deformation remains symmetric (top picture). When the beam power is increased, the growth of the deformation makes radiation pressure sensitive to incidence angles and then more efficient on the right than on the left. The deformation is thus attracted in the beam propagation direction and becomes non-axisymmetric (bottom picture).

All these results show that the morphology of nonlinear interface deformations driven by the radiation pressure of a laser wave is even richer than expected, opening the route towards future original experiments. Further developments on nonlinear effects, where a feedback coupling between deformation and propagation emerges, will extend deformation shapes to self-adapted ones as for liquid optical fibres [34] and nipple-like shapes observed experimentally [35]. They both involve light guiding within the deformation that modifies in turn the radiation pressure along the structure. This thorough analysis of optohydrodynamics provides the general frame to predict and anticipate further developments of contactless interface manipulation at the micrometer scale.

This research was supported by Centre National de la Recherche Scientifique (France), Université Bordeaux 1, and Conseil Régional d'Aquitaine (Contract No. 20051101010A). We thank Julien Petit for his contribution to fig. 10.

References

1. F.K. Wohlhuter, O.A. Basaran, *J. Fluid Mech.* **235**, 481 (1992).
2. J.D. Sherwood, *J. Fluid Mech.* **188**, 133 (1987).
3. A. Ashkin, J.M. Dziedzic, *Phys. Rev. Lett.* **30**, 139 (1973).
4. R.N.C. Pfeifer, T.A. Nieminen, N.R. Heckenberg, H. Rubinsztein-Dunlop, *Rev. Mod. Phys.* **79**, 1197 (2007).
5. J.Z. Zhang, R.K. Chang, *Opt. Lett.* **13**, 916 (1988).

6. A. Casner, J.P. Delville, Phys. Rev. Lett. **87**, 054503 (2001).
7. A. Casner, J.P. Delville, Phys. Rev. Lett. **90**, 144503 (2003).
8. K. Sakai, D. Mizuno, K. Takagi, Phys. Rev. E **63**, 046302 (2001).
9. S. Mitani, K. Sakai, Phys. Rev. E **66**, 031604 (2002).
10. Y. Yoshitake, S. Mitani, K. Sakai, K. Takagi, J. Appl. Phys. **97**, 024901 (2005).
11. F. Wottawah, S. Schinkinger, B. Lincoln, R. Ananthakrishnan, M. Romeyke, J. Guck, J. Kas, Phys. Rev. Lett. **94**, 098103 (2005).
12. A.V. Kats, I.S. Spevak, Sov. J. Quantum Electron. **9**, 857 (1979).
13. A. Casner, J.P. Delville, Opt. Lett. **26**, 18 (2001).
14. I.I. Komissarova, G.V. Ostrovskaya, E.N. Shedova, Opt. Commun. **66**, 15 (1988).
15. J.M. Hartings, X.Pu, J.L. Cheung, R.K. Chang, J. Opt. Soc. Am. B **14**, 2842 (1997).
16. E. Schäffer, T. Thurn-albrecht, T.P. Russel, U. Steiner, Nature **403**, 874 (2000).
17. R.Wunenburger, A.Casner, J.P. Delville, Phys. Rev. E **73**, 036314 (2006).
18. A. Hallanger, I. Brevik, S. Haaland, Phys. Rev. E **71**, 056601 (2005).
19. H. Chraïbi, D. Lasseux, E. Arquis, R. Wunenburger, J.P. Delville, Eur. J. Mech. B/Fluids **27**, 419 (2008).
20. J.A. Stratton, *Electromagnetic Theory* (McGraw-Hill, 1941).
21. R. Wunenburger, A. Casner, J.P. Delville, Phys. Rev. E **73**, 036315 (2006).
22. C. Pozrikidis, *Boundary Integral and Singularity Methods for Linearized Viscous Flow* (Cambridge University Press, 1992).
23. J. Tanzosh, M. Manga, H.A. Stone, Boundary Element Technol. **VI**, 19 (1992).
24. M. Manga, H.A. Stone, J. Fluid Mech. **287**, 279 (1994).
25. D.M. Koch, D.L. Koch, J. Fluid Mech. **287**, 251 (1994).
26. S.H. Lee, L.G. Leal, J. Fluid Mech. **87**, 81 (1982).
27. G. Graziani, Int. Engng Sci. **27**, 855 (1989).
28. P.J. Davis, P. Rabinowitz, *Methods of Numerical Integration*, (Academic Press, 1984).
29. A.A. Bakr, *The Boundary Integral Equation Method in Axisymmetric Stress Analysis Problems, Lect. Notes Engin.* (Springer-Verlag, 1986).
30. B. Jean-Jean, E. Freysz, A. Ducasse, B. Pouligny, Europhys. Lett. **7**, 219 (1988).
31. D. Beysens, A. Bourgou, P. Calmettes, Phys. Rev. A **26**, 3589 (1982).
32. L.D. Landau, E.M. Lifshitz, *Electrodynamics of Continuous Media* (Pergamon, Oxford, 1960).
33. G.V. Ostrovskaya, I.I. Komissarova, E.N. Shedova, Opt. Commun. **66**, 15 (1987).
34. E. Brasselet, R.Wunenburger, J.-P. Delville, Phys. Rev. Lett. **101**, 014501 (2008).
35. A. Casner, J.P. Delville, I. Brevik, J. Opt. Soc. Am. B **20**, 2355 (2003).